

WITNESSING THE BIRTH OF THE RED SEQUENCE: ALMA HIGH-RESOLUTION IMAGING OF [CII] AND DUST IN TWO INTERACTING ULTRA-RED STARBURSTS AT $Z = 4.425$

I. OTEO^{1,2}, R. J. IVISON^{2,1}, L. DUNNE^{1,3}, I. SMAIL⁴, M. SWINBANK^{4,5}, Z-Y. ZHANG^{1,2}, A. LEWIS¹, S. MADDOX^{1,3}, D. RIECHERS⁶, S. SERJEANT⁷, P. VAN DER WERF⁸, M. BREMER⁹, P. CIGAN³, D. L. CLEMENTS¹⁰, A. COORAY¹¹, H. DANNERBAUER¹², S. EALES³, E. IBAR¹³, H. MESSIAS¹⁴, M. J. MICHAŁOWSKI¹, I. PÉREZ-FOURNON^{15,16}, E. VAN KAMPEN²,

¹Institute for Astronomy, University of Edinburgh, Royal Observatory, Blackford Hill, Edinburgh EH9 3HJ UK

²European Southern Observatory, Karl-Schwarzschild-Str. 2, 85748 Garching, Germany

³School of Physics and Astronomy, Cardiff University, The Parade, Cardiff CF24 3AA, UK

⁴Centre for Extragalactic Astronomy, Department of Physics, Durham University, South Road, Durham DH1 3LE UK

⁵Institute for Computational Cosmology, Department of Physics, Durham University, South Road, Durham DH1 3LE, UK

⁶Department of Astronomy, Cornell University, Ithaca, NY 14853, USA

⁷Department of Physical Sciences, The Open University, Milton Keynes, MK7 6AA, UK

⁸Leiden Observatory, Leiden University, P.O. Box 9513, NL-2300 RA Leiden, The Netherlands

⁹H.H. Wills Physics Laboratory, University of Bristol, Tyndall Avenue, Bristol BS8 1TL, UK

¹⁰Physics Department, Blackett Lab, Imperial College, Prince Consort Road, London SW7 2AZ, UK

¹¹Department of Physics and Astronomy, University of California, Irvine, CA 92697

¹²Universität Wien, Institut für Astrophysik, Türkenschanzstrasse 17, 1180 Wien, Austria

¹³Instituto de Física y Astronomía, Universidad de Valparaíso, Avda. Gran Bretaña 1111, Valparaíso, Chile

¹⁴Centro de Astronomia e Astrofísica da Universidade de Lisboa, Observatório Astronómico de Lisboa, Tapada da Ajuda, 1349-018, Lisbon, Portugal

¹⁵Instituto de Astrofísica de Canarias, E-38205 La Laguna, Tenerife, Spain and

¹⁶Universidad de La Laguna, Dpto. Astrofísica, E-38206 La Laguna, Tenerife, Spain

Draft version March 4, 2022

ABSTRACT

Exploiting the sensitivity and spatial resolution of the Atacama Large Millimeter/submillimeter Array (ALMA), we have studied the morphology and the physical scale of the interstellar medium - both gas and dust - in SGP38326, an unlensed pair of interacting starbursts at $z = 4.425$. SGP38326 is the most luminous star bursting system known at $z > 4$ with an IR-derived SFR $\sim 4300 M_{\odot} \text{ yr}^{-1}$. SGP38326 also contains a molecular gas reservoir among the most massive ever found in the early Universe, and it is the likely progenitor of a massive, red-and-dead elliptical galaxy at $z \sim 3$. Probing scales of $\sim 0.1''$ or $\sim 800 \text{ pc}$ we find that the smooth distribution of the continuum emission from cool dust grains contrasts with the more irregular morphology of the gas, as traced by the [CII] fine structure emission. The gas is also extended over larger physical scales than the dust. The velocity information provided by the resolved [CII] emission reveals that the dynamics of the two components of SGP38326 are compatible with disk-like, ordered rotation, but also reveals an ISM which is turbulent and unstable. Our observations support a scenario where at least a subset of the most distant extreme starbursts are highly dissipative mergers of gas-rich galaxies.

Subject headings: galaxy evolution; sub-mm galaxies; dust emission; number counts

1. INTRODUCTION

Surveys in the far-infrared (FIR) and (sub)-mm have revolutionized our understanding of the formation and evolution of galaxies, revealing a population of dusty starbursts at $z > 1$ that are forming stars at tremendous rates (Blain et al. 2002; Chapman et al. 2005; Weiß et al. 2009; Geach et al. 2013; Casey et al. 2013). At $z > 4$ these starbursts can be linked to the formation of the so-called red-sequence – passively evolving, early type galaxies which dominate the cores of clusters out to at least $z \sim 1.5$ (e.g. Stanford et al. 2006; Rosati et al. 2009; Mei et al. 2009; Strazzullo et al. 2010; Tozzi et al. 2015). While the bulk of star formation in the *general* population of galaxies occurred in the period since $z \sim 2$ (Sobral et al. 2013), red-sequence galaxies at $z > 1.5$ formed the bulk of their stellar population at much earlier times and over a brief time interval (Thomas et al. 2005, 2010). Therefore, analysing strong starbursts at $z > 4$ is a way to study the likely progenitors of the most massive elliptical galaxies at $z > 1.5$ and, con-

sequently, the birth of the galaxy red sequence, which might have appeared as early as $z > 2$ (Kodama et al. 2007; Zirm et al. 2008; Kriek et al. 2008; Gabor & Davé 2012; Hartley et al. 2013).

Herschel extragalactic imaging surveys such as *Herschel*-ATLAS (Eales et al. 2010) and HerMES (Oliver et al. 2010) have covered about 1000 deg^2 to the SPIRE confusion limit. As a consequence, the number of known dusty starbursts has increased from several hundred to several hundred thousand. Most of these are at $z < 3$, but there is also a population of sources at $z > 4$. Dusty starbursts at $z > 4$ can be found by looking for galaxies whose far-IR (FIR) spectral energy distributions (SEDs) rise from $250 \mu\text{m}$ to $500 \mu\text{m}$, so their thermal dust emission peak is redshifted close to, or beyond $500 \mu\text{m}$. These are called $500 \mu\text{m}$ risers. Using *H*-ATLAS data, we have built a sample of dusty starbursts at $z > 4$ whose SPIRE flux densities satisfy $S_{500 \mu\text{m}}/S_{250 \mu\text{m}} > 2$ and $S_{500 \mu\text{m}}/S_{350 \mu\text{m}} > 1$, and we refer to these as ultrared starbursts (Ivison et al. in prep.). The resulting population was inspected by eye in each SPIRE band to exclude blended sources, checked for con-

tamination by radio-loud AGN and correlated with deep WHT/VISTA/Gemini optical/NIR imaging to reject any lenses that might have crept in despite our low median $S_{500\mu\text{m}}$ of ~ 50 mJy. Over 150 of these $500\mu\text{m}$ risers were followed up with SCUBA-2 (Holland et al. 2013) and LABOCA (Siringo et al. 2009) to improve FIR photometric redshifts and select only those whose colors are consistent with $z > 4$ by imposing $S_{870\mu\text{m}}/S_{500\mu\text{m}} > 0.4$.

In this paper we present ALMA high-spatial resolution ($\sim 0.1''$) observations of dust and gas (traced by [CII] emission) in HATLAS J000307–330250, also known as SGP38326, one of our ultra-red starbursts confirmed to be at $z = 4.425$ via multi-CO line detection. In §2 we give a description of the ALMA data used in this work and how they were reduced and analyzed. In §3 we present and discuss the main results of this work, regarding the properties of SGP38326: detected emission lines, the implied molecular gas mass, morphology of dust and atomic gas, etc. Finally, §4 summarizes the main conclusions of this work. The total IR luminosities (L_{IR}) reported in this work refer to the integrated luminosities between rest-frame 8 and $1000\mu\text{m}$. Throughout this paper, the reported SFRs are derived from the total IR luminosities ($L_{\text{IR},8-1000\mu\text{m}}$) assuming a Salpeter IMF and the Kennicutt (1998) calibration. Unless explicitly specified, the areas are calculated by carrying out 2D elliptical gaussian fits and using $A = \pi \times R_1 \times R_2$, where R_1 and R_2 are the semi axes of the best-fitting elliptical gaussians, $R_1 = \text{FWHM}_1/2$ and $R_2 = \text{FWHM}_2/2$. All values taken from the literature are re-scaled to be consistent. We assume a flat universe with $(\Omega_m, \Omega_\Lambda, h_0) = (0.3, 0.7, 0.7)$, and all magnitudes are listed in the AB system (Oke & Gunn 1983). For this cosmology, the sky scale is ~ 6.6 kpc/'' at $z = 4.425$, the redshift of SGP38326.

2. ALMA DATA

This work makes use of ALMA data from two different projects. Project 2013.1.00449.S was aimed at deriving redshifts via spectral scans in the ALMA 3mm window (PI. A. Conley) of a sample of ultra-red starbursts at $z > 4$ of which SGP38326 was a part. Project 2013.1.00001.S was a high-spatial resolution study of the dust continuum morphology at $870\mu\text{m}$ of a subsample of our ultra-red starbursts (PI. R.J. Ivison) of which SGP38326 was also a part. The ALMA data corresponding to the two projects were calibrated by using the ALMA pipeline and by executing different ALMA calibration scripts depending on the date when the data were released. The calibrated visibilities for the calibrators and science target were visually inspected and only very minor further flagging was required. The calibrated visibilities of the science target were then imaged in CASA by using a NATURAL weighting scheme to maximize sensitivity. The different tunings of the ALMA 3mm spectral scan were carried out at different dates with the array in different configurations. Therefore, the beam size is different for each tuning. In this work we only use the ALMA 3mm data corresponding to the tunings where the $^{12}\text{CO}(4-3)$ and $^{12}\text{CO}(5-4)$ lines were detected. The beam sizes were $1.5'' \times 1.2''$ and $1.1'' \times 1.0''$ for the $^{12}\text{CO}(4-3)$ and $^{12}\text{CO}(5-4)$ transitions, respectively. The r.m.s. of the $^{12}\text{CO}(4-3)$ and $^{12}\text{CO}(5-4)$ observations are 0.54 mJy beam $^{-1}$ and 0.64 mJy beam $^{-1}$, respectively,

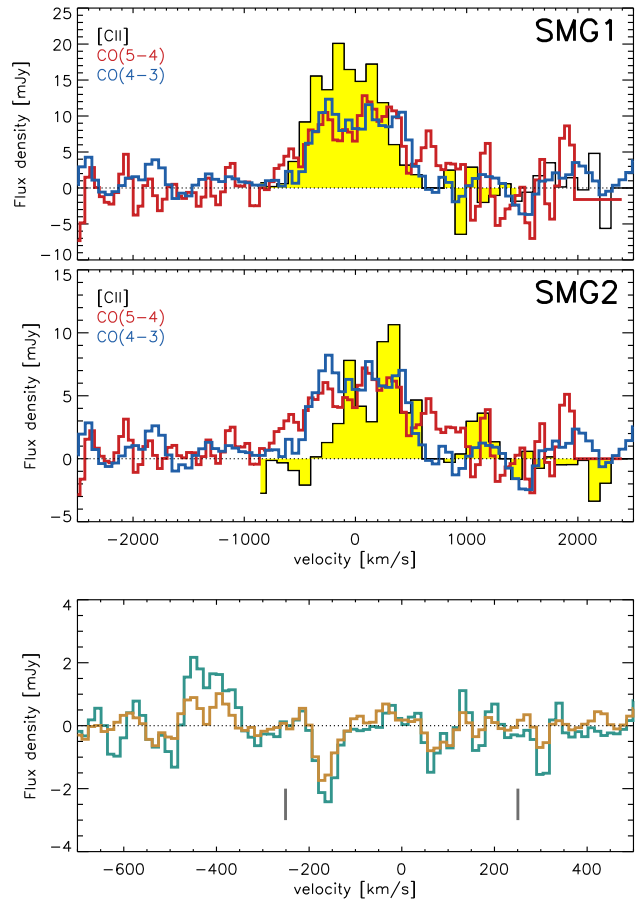


FIG. 1.— *Upper and middle*: Unambiguous confirmation that SGP38326 lies at $z = 4.425$ via detection of $^{12}\text{CO}(5-4)$ and $^{12}\text{CO}(4-3)$ in an ALMA 3mm spectral scan. The CO lines shown correspond to the emission of SMG1 and SMG2. The [CII] emission of the two interacting components of SGP38326 (see text for more details) are also shown. The CO spectra have been re-scaled (multiply by 3 for $^{12}\text{CO}(5-4)$ and 6 for $^{12}\text{CO}(4-3)$) to match the flux scale of the [CII] line. *Bottom*: Faint (or absent) OH $163\mu\text{m}$ emission in SMG1. The green curve represents the spectrum in the center of SMG1 (extracted from an aperture equal to one synthesized beam), where dust emission is at its maximum. The brown spectrum has been extracted using an aperture enclosing the whole area where [CII] emission is detected. Small vertical grey lines represent where the two components of the OH $163\mu\text{m}$ would be located assuming the redshift derived from the detected CO and [CII] lines. There is a narrow (81 ± 16 km s $^{-1}$, FWHM) emission line at ~ -400 km s $^{-1}$ at the center of SMG1 (where the dust continuum emission is at its maximum) that we tentatively associate to OH $163\mu\text{m}$ emission (see details in §3.5). No OH $163\mu\text{m}$ emission or absorption is detected in SMG2 either (spectrum not shown for the sake of representation clarity). In all panels, the spectra shown were extracted after continuum subtraction.

in 50 km/s channels. The beam size of the $870\mu\text{m}$ observations is $0.16'' \times 0.12''$, which corresponds to a physical scale of about 1.0 kpc \times 790 pc. The r.m.s. of the $870\mu\text{m}$ continuum map is 0.11 mJy beam $^{-1}$, while the r.m.s. in the spectral window where [CII] is detected is 0.66 mJy beam $^{-1}$ in 100 km/s channels.

3. SGP38326: A PAIR OF INTERACTING STARBURSTS AT $Z = 4.425$

SGP38326 was selected in the Southern field of the *Herschel*-ATLAS (Eales et al. 2010, Valiante et al. in prep) as a $500\mu\text{m}$ riser (see §1). The SPIRE flux densities of SGP38326 are $S_{250\mu\text{m}} = 28.6 \pm 5.2$ mJy, $S_{350\mu\text{m}} =$

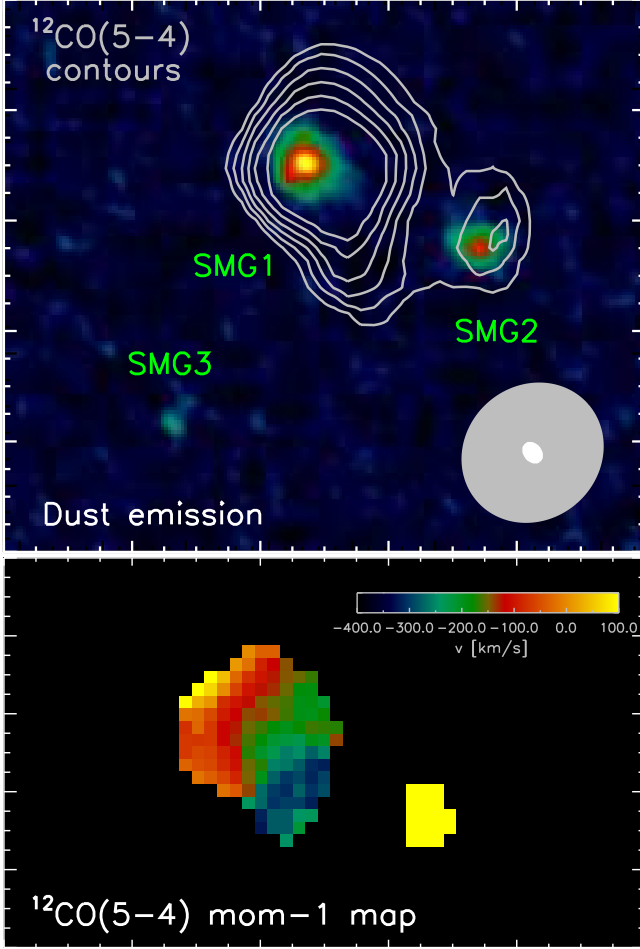


FIG. 2.— *Upper*: ALMA 870 μm continuum map of SGP38326. The three detected SMGs are indicated. The grey contours represent the integrated $^{12}\text{CO}(5-4)$ emission. This line is clearly detected in both SMG1 and SMG2, but there is no $^{12}\text{CO}(5-4)$ detection in SMG3. The beam sizes of the $^{12}\text{CO}(5-4)$ (grey ellipse, $1.1'' \times 1.0''$) and dust continuum (white ellipse, $0.16'' \times 0.12''$) observations are shown, and clearly highlight the impressive increase in spatial resolution. *Bottom*: Velocity map of SMG1 derived from the $^{12}\text{CO}(5-4)$ emission using moment masking (Dame 2011). It can be seen that, despite the lack of spatial resolution, the $^{12}\text{CO}(5-4)$ observations already indicate that SMG1 presents a disk-like rotation. In both panels, north is up and east is left.

$28.6 \pm 5.8 \text{ mJy}$, $S_{500\mu\text{m}} = 46.2 \pm 6.8 \text{ mJy}$. SGP38326 was subsequently observed with SCUBA-2 at $870 \mu\text{m}$ ($S_{870\mu\text{m}} = 32.5 \pm 4.1 \text{ mJy}$) and, by fitting a set of FIR templates to its SPIRE and SCUBA-2 flux densities, we determined a best-fit photometric redshift $z_{\text{phot}} \sim 4.5$.

The ALMA spectral scan in the 3mm window confirmed its redshift to be $z = 4.425 \pm 0.001$ via detection of the $^{12}\text{CO}(4-3)$ and $^{12}\text{CO}(5-4)$ emission lines (Fig. 1). The total IR luminosity of SGP38326, obtained from an SED fit to the *Herschel* and SCUBA-2 flux densities, is $L_{\text{IR}}/L_{\odot} \sim 2.5 \times 10^{13}$, implying a staggering IR-derived SFR $\sim 4300 M_{\odot} \text{ yr}^{-1}$, among the strongest starbursts so far found in the early Universe (see Table 1). The CO emission lines are extremely wide, $\text{FWHM}_{^{12}\text{CO}(4-3)} = 1081 \pm 91 \text{ km s}^{-1}$ and $\text{FWHM}_{^{12}\text{CO}(5-4)} = 1278 \pm 84 \text{ km s}^{-1}$, from gaussian fits. This is compatible with SGP38326 being a system of

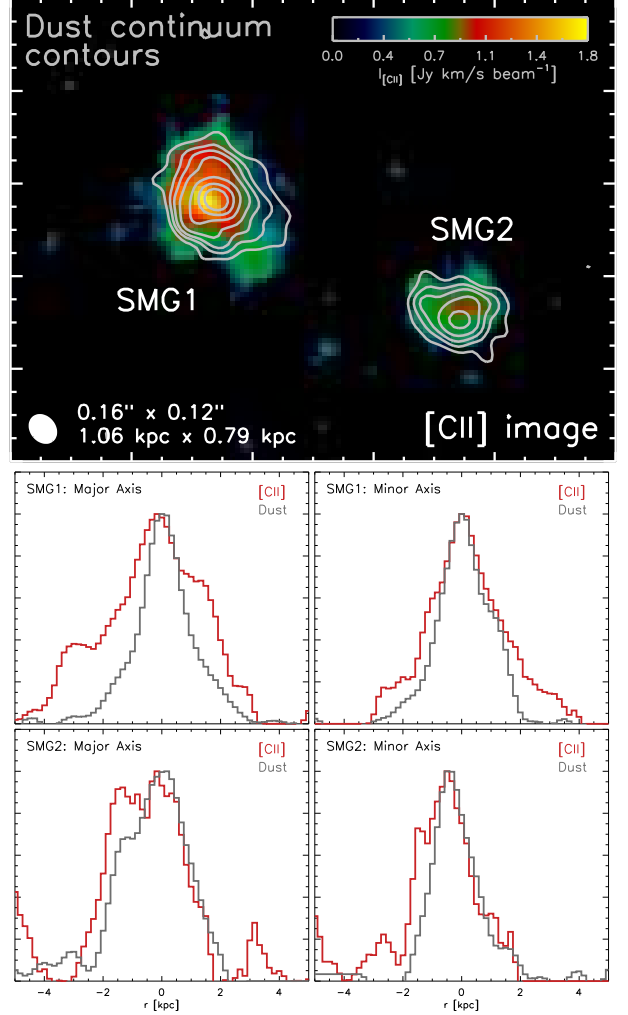


FIG. 3.— Morphology and spatial extent of the gas and dust in our two distant interacting starbursts. In the top panel, the background image is the integrated [CII] emission created by using moment masking (Dame 2011), while grey contours represent dust emission at rest-frame $160\mu\text{m}$. Contours are plotted from 3σ to 7σ in steps of 2σ and from 10σ to 25σ in steps of 5σ , where $\sigma = 0.11 \text{ mJy beam}^{-1}$. The two interacting galaxies are separated by a physical distance of $\sim 10 \text{ kpc}$. The beam size is also included. It can be seen that the dust continuum is smooth at the resolution of these data. However, the gas reservoir (as traced by [CII] emission) has an irregular morphology and is extended over larger physical scales. In this panel, north is up and east is left. The bottom panels show the radial profiles (normalized units) of dust and gas along the [CII] major and minor axes of each starburst. It can be seen that the profiles are significantly different, with [CII] emission being more extended than dust, especially in SMG1.

at least two starbursts in the process of interaction, as already seen in extreme starbursts at lower redshifts with similarly wide CO lines (Fu et al. 2013; Ivison et al. 2013). In fact, the $^{12}\text{CO}(5-4)$ observations resolved SGP38326 into two interacting components, SMG1 and SMG2 (see Figure 2). The $^{12}\text{CO}(5-4)$ emission in SMG1 presents an elongated extension towards the south. This can be interpreted as a faint and relatively dust poor CO emitter interacting with SMG1 and SMG2, a CO bridge connecting the two interacting components (see also later in the text), or an outflow. The depth and resolution of the data are insufficient to fully discriminate between the possible scenarios. As discussed later, the [CII] ve-

locity map shows no evidence of outflowing atomic gas and OH 163 μm emission (a tracer of molecular outflows) is not clearly detected in SMG1 despite the detection of the continuum at the line frequency. The existence of a CO bridge is supported by the detection of similar structures in other systems of interacting starbursts at lower redshifts (Zhu et al. 2007; Fu et al. 2013; Appleton et al. 2015) and QSOs (Carilli et al. 2013). The velocity map of SMG1 obtained from the $^{12}\text{CO}(5-4)$ emission is compatible with an ordered rotation (see Figure 2). As shown in §3.6, this velocity structure is in agreement with that obtained from the [CII] emission at $\sim 10\times$ times better spatial resolution (see §3.6).

SGP38326 is resolved into three 870 μm components (see Figure 2), as are many bright SMGs (Karim et al. 2013; Hodge et al. 2013; Simpson et al. 2015a,b; Bussmann et al. 2015). SMG1 and SMG2 (Fig. 3), the brightest components (see flux densities in Table 2), are both at the same redshift, $z = 4.425$. There is no [CII] or CO emission detected in SMG3 ($S_{870\mu\text{m}}^{\text{SMG3}} = 1.7 \pm 0.4 \text{ mJy}$), located 2.2'' away from SMG1. This might indicate that SMG3 has a different redshift than SMG1 and SMG2. However, SMG3 is about 14 times fainter than the SMG1 and SMG2 combined. If we assume that the CO luminosity scales with the total IR luminosity, the peak flux of the CO lines would be much lower than the r.m.s. of the observations. The same is true for [CII] assuming again that its luminosity scales with the total IR luminosity. Therefore, with the current data, is not possible to clarify whether SMG3 is also interacting with SMG1 and SMG2. From now on, we focus our study on SMG1 and SMG2, the two clear components of the merging system. These are separated by $\sim 10 \text{ kpc}$ in the plane of the sky and their properties are summarized in Table 2.

Due to the high inferred luminosity of SGP38326, we should consider whether its emission has been amplified by gravitational lensing. SGP38326 has no near-IR counterpart in the VIKING survey (Edge et al. 2013); the closest VIKING-detected source is $\sim 7.5''$ away. The 5σ limiting magnitudes of the VIKING survey range from 23.1 mag in the Z band to 21.2 mag in the K_s band. Assuming that any lens galaxy would be an elliptical, the limiting magnitude in Z would imply $I < 23.1 \text{ mag}$. Therefore, the lack of VIKING detection would imply that any potential lensing galaxy would be significantly fainter than the lenses in the H-ATLAS survey discovered so far (Bussmann et al. 2013). Additionally, the dust continuum emission does not show any evidence of lensing, as it does in some ultra-red starburst at $z > 4$ (Oteo et al. in prep). Therefore, neither of the two merging components is lensed, in contrast with other high- z extremely bright galaxies reported in the literature, such as HFLS3 (Riechers et al. 2013; Cooray et al. 2014), HDF 850.1 (Walter et al. 2012), HXMM01 (Fu et al. 2013) or HATLAS J084933 (Iverson et al. 2013).

3.1. A massive molecular gas reservoir

The integrated $^{12}\text{CO}(5-4)$ emission shown in Figure 2 can be used to estimate the total mass of the molecular gas reservoir in SGP38326, as well as the molecular gas mass of each interacting component. Low- J CO lines are much better tracers of the total molec-

ular gas mass than the mid- J CO lines (the ones detected in our ALMA 3mm spectral scan), which trace only a relatively dense component. Therefore, we need to assume that the average CO line ratio for SMGs (Carilli & Walter 2013), $L'_{\text{CO}(5-4)}/L'_{\text{CO}(1-0)} = 0.39$, is valid for SGP38326. The molecular gas masses are then calculated using $\alpha_{\text{CO}} = 0.8 M_{\odot} (\text{K km s}^{-1} \text{ pc}^2)$, a value typically assumed for high- z starbursts and local ULIRGs (Downes & Solomon 1998). The derived values are shown in Table 2. The total molecular gas of SGP38326 ($M_{\text{g, total}} = M_{\text{g}}^{\text{SMG1}} + M_{\text{g}}^{\text{SMG2}}$ - see also Table 1) is higher than that in any other system so far studied at similar redshifts (see Table 1). We note that the calculation of the molecular gas mass from a single mid- J transition might be highly uncertain due to the effect that variation in excitation has on the CO line ratios. Further observations of low- J CO transitions would thus be needed to confirm whether the high luminosity of the $^{12}\text{CO}(5-4)$ transition is due to the presence of a very massive molecular gas reservoir rather than a highly excited gas component.

3.2. Dust continuum morphology

Although SGP38326 is resolved into two interacting galaxies, each of them is an extremely luminous starburst in its own right. The dust continuum emission of SMG1 and SMG2 (rest-frame 160 μm) is relatively smooth (see grey contours in Fig. 3). At this spatial resolution, there is no clear evidence of clumpy emission in SMG1 and SMG2. The physical extent of the dust emission has been measured from a two-dimensional elliptical gaussian profile fit. Table 2 shows the FWHM of the major and minor axis of each of the components of SGP38326. These values are at the high-end of the size distribution of lower-redshift SMGs (Simpson et al. 2015a) and compatible with the size of $z > 3$ SMGs in Ikarashi et al. (2015). SMG1 and SMG2 are, however, considerably smaller than the dust emission in GN20: $\sim 5.3 \text{ kpc} \times 2.3 \text{ kpc}$ (Hodge et al. 2015).

Their size in combination with their IR-derived SFR (see Table 2) imply that SMG1 and SMG2 have median SFR surface densities of $\Sigma_{\text{SFR}} \sim 840 M_{\odot} \text{ yr}^{-1} \text{ kpc}^{-2}$ and $\Sigma_{\text{SFR}} \sim 570 M_{\odot} \text{ yr}^{-1} \text{ kpc}^{-2}$, respectively. The Σ_{SFR} of SMG1 is very close to the theoretically predicted Eddington limit for starburst disks that are supported by radiation pressure (Andrews & Thompson 2011; Simpson et al. 2015b). Such high Σ_{SFR} values have been only found in the $z = 6.42$ quasar host galaxy J1148+5251 (Walter et al. 2009) and the dusty starbursts HFLS3 at $z = 6.34$ (Riechers et al. 2013) and AzTEC-3 at $z \sim 5.3$ (Riechers et al. 2014) and are considerably higher than the Σ_{SFR} found in other starbursts at similar redshifts (see Table 1).

Combining the sizes of the dust emission with the molecular gas mass estimates (assuming the molecular gas and dust are roughly co-spatial), we find that the estimated gas surface density of SMG1 and SMG2 are among the highest ever found (see Table 2). The values found for the SFR surface density, in combination with the derived gas mass surface densities place SMG1 and SMG2 between the sequence of starbursts and 'normal' star-forming galaxies in the $\Sigma_{\text{SFR}} - \Sigma_{\text{H}_2}$ plane, with gas depletion time scales between 10 and 100 Myr (Hodge et al.

TABLE 1
 PROPERTIES OF SGP38326 COMPARED TO OTHER IR-BRIGHT STARBURSTS IN THE DISTANT UNIVERSE.

Source	redshift	$S_{870\mu\text{m}}$ [mJy]	SFR [$M_{\odot} \text{ yr}^{-1}$]	M_{H_2} [M_{\odot}] ^a	Σ_{SFR} [$M_{\odot} \text{ yr}^{-1} \text{ kpc}^{-2}$]	Lensed? ^b	Reference
SGP38326	4.425	32.5 ± 4.1	$\sim 4300^{\text{c}}$	$\sim 2.7 \times 10^{11}$	$\sim 840 / \sim 570^{\text{d}}$	No	This work
GN20	4.055	20.3 ± 2.1	~ 3000	$\sim 1.3 \times 10^{11}$	~ 310	No	Hodge et al. (2012)
HDF 850.1	5.183	7.0 ± 0.4	~ 850	$\sim 3.5 \times 10^{10}$	~ 50	Weakly	Walter et al. (2012)
AzTEC-3	5.299	$6.20 \pm 0.25^{\text{e}}$	~ 1980	$\sim 5.3 \times 10^{10}$	~ 840	No	Riechers et al. (2014)
HFLS3	6.337	14.3 ± 1.1	~ 2100	$\sim 3.6 \times 10^{10}$	~ 600	Weakly	Riechers et al. (2013)

^aMolecular gas masses reported assume an $\alpha_{\text{CO}} = M_{\text{gas}}/L'_{\text{CO}} = 0.8 \text{ K km s}^{-1} \text{ pc}^2$, typical for high-redshift starbursts and local ULIRGs (Downes & Solomon 1998). Values taken from the literature have been scaled accordingly.

^bFor lensed galaxies, de-magnified values are listed.

^cTotal SFR in SGP38326: $\text{SFR} = \text{SFR}_{\text{SMG1}} + \text{SFR}_{\text{SMG2}}$.

^dValues for SMG1 and SMG2 are given.

^eMeasured at 1mm.

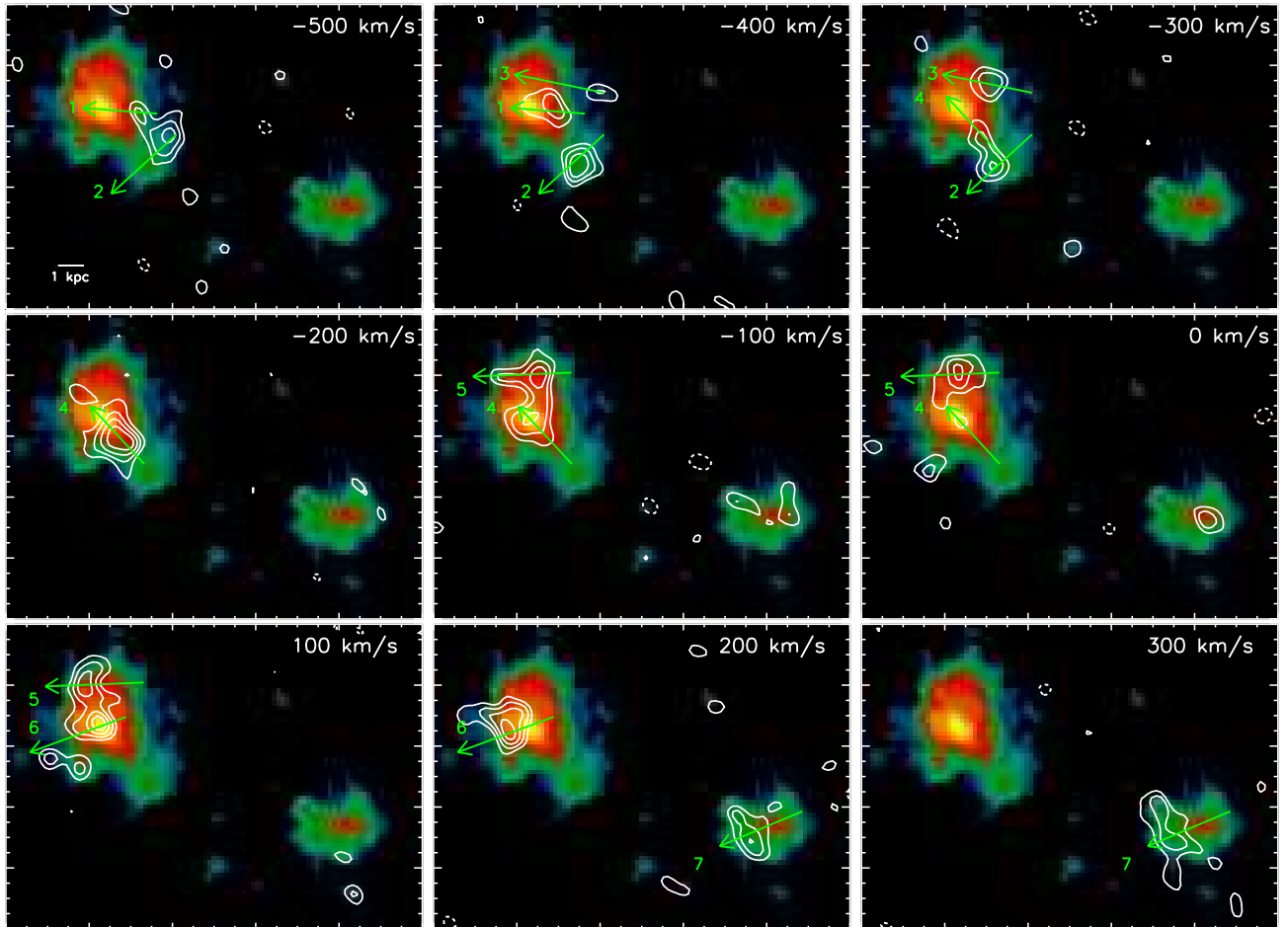


FIG. 4.— Dynamics of SGP38326 at high-spatial resolution from [CII] emission: [CII] velocity channel contours are overlaid on the [CII] moment-0 map. The velocity channels have been averaged over 100 km s^{-1} . Contours in the velocity channels start at $\pm 3\sigma$ and are represented in steps of 1σ ($1\sigma = 0.66 \text{ mJy beam}^{-1}$). Green arrows and associated numbers indicate the velocity gradients identified in the continuum-subtracted [CII] data cube.

2015). However, it should be noted that this result assumes that the average CO line ratios for SMGs are valid for SGP38326.

3.3. Dust properties and SED fitting

The SPIRE fluxes for SMG1 and SMG2 are blended within the large SPIRE beam and the signal-to-noise ratio in the image is not high enough to attempt to deblend them using the ALMA $870\mu\text{m}$ positions. Instead we fit the global SED of both sources using both opti-

cally thin and optically thick modified black bodies to derive the dust temperatures and dust masses, as well as the integrated IR luminosity. To get the values for each source separately we have assumed they have the same SED shape and split the IR luminosity and dust mass in the ratio of the $870\mu\text{m}$ fluxes. Table 2 lists the dust and SED properties. Because of the relatively low SNR of the SPIRE $250\mu\text{m}$ measurement and only upper limits for PACS, we have no strong preference for either an optically thin or optically thick model, both

TABLE 2
OBSERVED PROPERTIES OF OUR TWO INTERACTING DUSTY
STARBURSTS

	SMG1	SMG2
z_{spec}	4.4237 ± 0.0004	4.4289 ± 0.0004
$S_{870\mu\text{m}}^{\text{a}}$	$16.3 \pm 1.1 \text{ mJy}$	$7.3 \pm 0.5 \text{ mJy}$
$I_{[\text{CII}]} [\text{Jy km s}^{-1}]$	13.9 ± 1.1	5.3 ± 0.6
$\Delta v_{[\text{CII}]} [\text{km s}^{-1}]$	626 ± 60	585 ± 95
$L_{\text{IR}} [L_{\odot}]$	$(1.6 \pm 0.3) \times 10^{13}$	$(7.9 \pm 0.3) \times 10^{12}$
SFR [$M_{\odot} \text{ yr}^{-1}$]	~ 2900	~ 1400
$A_{\text{dust}} [\text{kpc}^2]^{\text{b}}$	$2.2 \pm 0.2 \times 2.0 \pm 0.2$	$2.1 \pm 0.2 \times 1.5 \pm 0.1$
$A_{[\text{CII}]} [\text{kpc}^2]^{\text{b}}$	$3.8 \pm 0.1 \times 2.9 \pm 0.1$	$2.7 \pm 0.1 \times 2.1 \pm 0.1$
$\Sigma_{\text{SFR}} [M_{\odot} \text{ yr}^{-1} \text{ kpc}^{-2}]$	~ 840	~ 570
$M_{\text{H}_2} [M_{\odot}]$	$\sim 1.9 \times 10^{11}$	$\sim 7.6 \times 10^{10}$
$M_{\text{dust}}^{\text{c}} [M_{\odot}]$	$\sim 1.9 \times 10^9$	$\sim 6.9 \times 10^8$
$\Sigma_{\text{H}_2} [M_{\odot} \text{ pc}^{-2}]$	$\sim 5.6 \times 10^4$	$\sim 3.1 \times 10^4$
$T_{\text{dust}}^{\text{c}} [\text{K}]$	~ 33	~ 34
$L_{[\text{CII}]} [L_{\odot}]$	$(8.3 \pm 0.2) \times 10^9$	$(2.9 \pm 0.2) \times 10^9$

^aFlux densities derived from the ALMA $870\mu\text{m}$ observations (§2) after primary beam attenuation correction. At the high signal to noise of the $870\mu\text{m}$ detections, the effect of flux boosting is negligible (Oteo et al. 2015).

^bThe reported values of the size of dust and [CII] emission are $\text{FWHM}_{\text{major}} \times \text{FWHM}_{\text{minor}}$, where $\text{FWHM}_{\text{major}}$ and $\text{FWHM}_{\text{minor}}$ are obtained from a two-dimensional elliptical gaussian profile fit to the observed emission.

^cValues obtained assuming optically thin models

produce acceptable fits with comparable L_{IR} . What differs strongly between the two models is the dust temperature and accordingly the dust mass which, for a rest frame continuum measurement of $160\mu\text{m}$, is strongly sensitive to the assumed dust temperature. The optically thin model gives a best fit temperature of 33 ± 2 K, and dust masses of $M_{\text{d}}(\text{SMG1}) = 1.9 \times 10^9 M_{\odot}$ and $M_{\text{d}}(\text{SMG2}) = 6.9 \times 10^8 M_{\odot}$, using a value of $\beta = 2$ and $\kappa_{850} = 0.077 \text{ m}^2/\text{kg}^{-1}$ (Dunne & Eales 2001). This dust temperature would be remarkably low for such a highly star forming galaxy in the local Universe but it is now well established that high- z SMGs have much cooler SEDs for their infrared luminosity than do local ULIRGs, due to the more widespread nature of their star formation (Hwang et al. 2010; Elbaz et al. 2011; Symeonidis et al. 2013). The optically thick fit gives a higher dust temperature of 55 K with a correspondingly lower dust mass of $5.6 \times 10^8 M_{\odot}$ and $2.1 \times 10^8 M_{\odot}$ for SMG1 and SMG2 respectively. The optical depth at $100\mu\text{m}$ is $\tau_{100} \sim 3$ in both galaxies. Dust is a good tracer of molecular gas at both high and low redshift and is increasingly being used as an alternative to, or consistency check for CO derived measurements (Rowlands et al. 2014; Scoville et al. 2015; Berta et al. 2015). The derived gas mass and optically thin dust masses imply gas to dust ratios of $M_{\text{g}}/M_{\text{d}} \sim 101$ and ~ 110 for SMG1 and SMG2, respectively. These values are compatible with those found for starbursts at similar redshifts (Magdis et al. 2011), $z \sim 0.5 - 1.5$ main-sequence galaxies and classical SMGs (Magdis et al. 2012), local star forming spirals (Leroy et al. 2011; Sandstrom et al. 2013) and local LIRGs and ULIRGs (Solomon et al. 1997; Dunne & Eales 2001).

If we instead use the optically thick mass estimates we find higher gas-to-dust ratios by a factor ~ 3 , but in the extreme conditions of these starbursts it would not be surprising to find both optically thick dust SEDs and

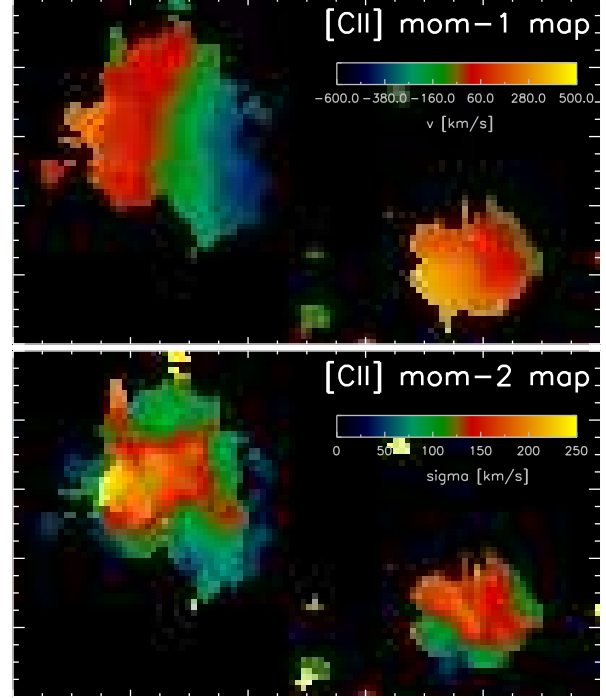


FIG. 5.— Resolved velocity (*upper*) and velocity dispersion (*bottom*) maps of the two interacting components in SGP38326 obtained from their [CII] emission by using moment masking (Dame 2011). As Figure 4 suggests, all velocity gradients found in SMG1 and SMG2 are compatible with ordered rotation although with some perturbations, likely due to the effect of the ongoing merger. highly excited molecular gas, both of which would lower the estimated molecular gas content by a factor of a few.

3.4. Morphology of [CII] emission

The redshift of SGP38326 was unknown when the $870\mu\text{m}$ continuum ALMA observations were performed. Fortunately, its redshifted [CII] emission was covered by the default continuum setup, offering a unique opportunity to study the ISM of intense starbursts at $z > 4$ at unprecedented spatial resolution.

The [CII] spectrum of the two merging components of SGP38326 is shown in Figure 1. SMG1 has a broad [CII] line ($626 \pm 60 \text{ km s}^{-1}$ FWHM, $L_{[\text{CII}]} / L_{\odot} = (8.3 \pm 0.2) \times 10^9$), considerably broader than the [CII] emission in other SMGs at similar redshifts (Swinbank et al. 2012; Walter et al. 2012; De Breuck et al. 2014; Riechers et al. 2014) and also broader than local ULIRGs (Farrah et al. 2013). The [CII] emission from SMG2 is slightly narrower ($585 \pm 95 \text{ km s}^{-1}$ FWHM, $L_{[\text{CII}]} / L_{\odot} = (2.9 \pm 0.2) \times 10^9$), with its center shifted $\sim 300 \text{ km s}^{-1}$ with respect to SMG1. The [CII] emission in SMG1 and SMG2 implies that their redshifts are $z_{\text{SMG1}} = 4.4237 \pm 0.0004$ and $z_{\text{SMG2}} = 4.4289 \pm 0.0004$, respectively. The escape velocity of the system (assuming a mass at least as high as the molecular gas mass) is significantly greater than the velocity offset between SMG1 and SMG2, meaning that the galaxies are destined to merge, in contrast to multiple HyLIRGs seen at lower redshifts (Ivison et al. 2013). Therefore, our results support a scenario where at least a subset of the most distant starbursts formed in

the same highly dissipative mergers of gas-rich galaxies that seem ubiquitous amongst SMGs at $z < 3$ and local ULIRGs (Engel et al. 2010). This result is an agreement with (Narayanan et al. 2015), which reported that major mergers are common at $z > 4$ and indeed drive some short-lived burst in star formation.

The smooth dust morphology contrasts with the more irregular [CII] emission (Fig. 3). [CII] can be associated with many ISM phases, such as photodissociation regions associated with star formation (Stacey et al. 1999), the diffuse or dense molecular medium (Wolfire et al. 2010) and atomic and ionized gas (Madden et al. 1997). Additionally, [CII] can be enhanced by shocks (Appleton et al. 2013) and altered by outflows (Cicone et al. 2015). In the [CII] velocity maps shown in Figure 4 there is no evidence for atomic outflows. Therefore, shock enhancement, local star formation conditions and tidal forces triggered by the interaction between the components, coupled with local excitation differences are the most likely explanations of the different morphologies of [CII] and dust.

Figure 3 also shows the profiles of the [CII] and dust emission along the major and minor axis of the [CII] emission of each starburst. In addition to their different morphology, the gas traced by [CII] is extended over larger physical scales than the dust (Tacconi et al. 2006; Ivison et al. 2011) and also has significantly different radial profiles. This is further supported by the same 2D gaussian fitting used to determine the size of the dust emission. The size of the [CII] emission is $3.8 \pm 0.1 \text{ kpc} \times 2.9 \pm 0.1 \text{ kpc}$ in SMG1 and $2.7 \pm 0.1 \text{ kpc} \times 2.1 \pm 0.1 \text{ kpc}$ in SMG2 (FWHM values are quoted here). Therefore, we find that [CII] is extended over a spatial scale larger than that found for dust (§3.2). This is in agreement to what it has been reported in other $z > 4$ sources, such as AzTEC-3 (Riechers et al. 2014), HFLS3 (Riechers et al. 2013), and W2246-0526 (Diaz-Santos et al. 2015), but at lower spatial resolution compared with the extension of the emission. Interestingly, some faint, tidal [CII] emission seems to be flowing from SMG1 to SMG2 as a consequence of their interaction. If confirmed, this would be similar to the CO and [CII] bridges that have been previously seen in other interacting starbursting systems (Fu et al. 2013; Carilli et al. 2013).

3.5. OH 163 μm emission

The default continuum observations also covered the 163 μm OH($^2\Pi_{1/2}J = 3/2 \rightarrow 1/2$) doublet (whose components are at $\nu_{\text{rest}} = 1834.74735$ and 1834.74735 GHz). We note that the nearby $^{12}\text{CO}(16-15)$ emission line is out of the spectral range covered. We present in Figure 1 the OH spectrum of SMG1 extracted in the area where dust emission is detected (brown spectrum). We also show (blue spectrum) the OH spectrum of SMG1 extracted on the position where the dust emission peaks and using an aperture the size of the synthesized beam. Assuming the redshift determined by the CO lines, the two components of the OH doublet should be located at the velocities marked by the short vertical grey lines. Despite the clear detection of the continuum, no OH emission is detected at the expected velocities. However, there is an emission line in the blue spectrum shifted by $\sim 200 \text{ km s}^{-1}$ blue-ward that might be associated with the OH doublet

since there is no other emission line that could lie at that frequency. An absorption line is apparent in the spectrum of SMG1 $\sim 100 \text{ km s}^{-1}$ red-ward of the expected position of any OH emission. However, the centers of the emission and absorption do not match with the redshifted components of the OH doublet. After continuum subtraction, Riechers et al. (2014) derived for AzTEC-3 a [CII] peak flux of about 18 mJy and a [OH] peak flux of about 2 mJy. This means a ratio of [CII]/OH ~ 10 . The peak [CII] flux in SMG1 is $\sim 20 \text{ mJy}$ and, assuming the same [CII]/OH ratio as in AzTEC-3, we would expect the OH emission to have a peak line flux of $\sim 2 \text{ mJy}$, in agreement with the peak flux of the emission line seen in the bottom panel of Figure 1. If the detected emission line is actually one of the OH components, its width ($\sim 85 \text{ km s}^{-1}$) is lower than that previously found in strong starbursts in the distant Universe (Riechers et al. 2013, 2014). We note that these are the only two cases where OH 163 μm emission has been clearly detected in $z > 4$ starbursts. The putative OH emission in SMG1 is also very compact, being spatially coincident with the maximum of the dust continuum emission. It should be pointed out that the OH emission is only seen where the dust emission is maximum. In contrast, the absorption is seen across the whole disk (brown spectrum in Figure 1).

3.6. Dynamics at high resolution from [CII] emission

The signal-to-noise of the [CII] detection allows us to study the dynamics of SMG1 and SMG2 to a level of detail never previously achieved for any $z > 4$ unlensed starburst. We present in Figure 4 the [CII] emission in all the velocity channels where it is detected. We have identified six different velocity gradients in SMG1 and one in SMG2, which reveal that both components of SGP38326 are ordered rotating disks, as corroborated by the [CII] velocity and velocity dispersion maps shown in Figure 5. It should be noted that the velocity field derived in SMG1 from [CII] is very similar to that obtained from the $^{12}\text{CO}(5-4)$ transition (see Figure 2), but with about 10x times better spatial resolution. We have fitted the observed velocity field using a disk plus dark matter halo model. We should note that, since the rotation curve does not turn over, the disk+halo model is degenerate. In any case, if it is a settled disk, it must be massive, with $v_c \sim 300 \text{ km s}^{-1}$ and with a best-fit inclination of ~ 65 deg. This suggests a dynamical mass $M_{\text{dyn, SMG1}} \sim 5 \times 10^{10} M_{\odot}$. The dynamical analysis from [CII] emission at high-spatial resolution indicates that the wide, unresolved CO emissions in SGP38326 (see Figure 1) are driven by the interaction of two disks separated by $\sim 200 \text{ km/s}$ in velocity space. This is opposite to, for example, to AzTEC-3, where the [CII] emission (which has half the width of the [CII] emission in SMG1) is supported by emission from a highly dispersed gas (Riechers et al. 2014).

It should be pointed out that the derived dynamical mass is $\sim \times 5$ lower than the molecular gas mass estimated either from CO or the optically thin dust SED fit. However, there are considerable uncertainties involved in the calculation of both of these quantities. The dynamical mass estimate is uncertain by at least by a factor of ~ 2 due to the uncertainty in the inclination of the disk and the merger state. The estimation of the molec-

ular gas mass assumes an α_{CO} factor (we used the value typically assumed for ULIRGs, see above) and a ratio between the $^{12}\text{CO}(5-4)$ and $^{12}\text{CO}(1-0)$ transitions. The derived molecular gas mass would be lower than the obtained value if α_{CO} is actually lower or if the mid- J CO lines are more excited than the average SMG.

We have also determined the dynamical mass of SMG1 and SMG2 by using the isotropic virial estimator (Tacconi et al. 2008; Förster Schreiber et al. 2009; Engel et al. 2010):

$$M_{\text{dyn, vir}} = 2.8 \times 10^5 \Delta v_{\text{FWHM}}^2 R_{1/2} \quad (1)$$

where Δv_{FWHM} is the width of the integrated [CII] line of each component and $R_{1/2}$ is the radius of the size of the [CII] emission. Since the size of the [CII] emission in SMG1 and SMG2 was derived by assuming elliptical gaussian profiles (see §3.4), $R_{1/2}$ is assumed to be the average value of the semi major and minor axis (measured from FWHM). The derived dynamical masses with this method for SMG1 and SMG2 ($M_{\text{dyn}}^{\text{SMG1}} \sim 3.6 \times 10^{11} M_{\odot}$ and $M_{\text{dyn}}^{\text{SMG2}} \sim 2.3 \times 10^{11} M_{\odot}$) are now higher than the molecular gas masses. As pointed out in Engel et al. (2010), the scaling factor appropriate for a rotating disk at an average inclination is a factor of ~ 1.5 smaller (Bothwell et al. 2010). Applying this correction to our measurements, the derived dynamical masses would still be higher than the molecular gas masses. In any case, to carry out a meaningful comparison between the molecular gas and dynamical mass and put constraints on the α_{CO} conversion factor, low- J CO observations would be needed.

We now examine whether the two disks in SGP38326 are stable by using the Toomre parameter Q (Toomre 1964), which characterizes the stability of a disk against gravitational fragmentation. In this sense, a disk is stable if $Q > 1$. We calculate the Toomre parameter by following Swinbank et al. (2015): $Q = \sigma_r \kappa / \pi G \Sigma_{\text{gas}}$, where $\kappa = a V_{\text{max}} / R$ is the epicyclic frequency (with $a = \sqrt{3}$), σ_r is the radial velocity dispersion, and Σ_{gas} is the gas mass surface density. All the dynamical parameters are obtained from the [CII] emission. We obtain $Q^{\text{SMG1}} \sim 0.22$ and $Q^{\text{SMG2}} \sim 0.35$, indicating that the two disks are unstable. For comparison, Swinbank et al. (2015) obtained $Q = 0.30 \pm 0.10$ for SDP.81, a strongly lensed galaxy at $z \sim 3$ observed with ALMA at very high spatial resolution (ALMA Partnership et al. 2015; Dye et al. 2015), while De Breuck et al. (2014) obtained an average $Q = 0.58 \pm 0.15$ for a $z \sim 4.8$ starburst containing an AGN. It should be noted that the derived value of the Toomre parameters relies on the validity for SGP38326 of the average CO line ratio for SMGs. This uncertainty is also present in previous works (Swinbank et al. 2015; De Breuck et al. 2014).

3.7. The spatially resolved $L_{\text{[CII]}}/L_{\text{IR}}$ ratio

Our high-spatial resolution observations also allow us to obtain the first resolved $L_{\text{[CII]}}/L_{\text{IR}}$ ratio map in a dusty starburst at $z > 4$. We have obtained the $L_{\text{[CII]}}/L_{\text{IR}}$ ratio map by simply dividing the $L_{\text{[CII]}}$ and L_{IR} maps. It should be noted that no convolution is required since the spatial resolution of the [CII] and dust continuum map is the same. The $L_{\text{[CII]}}$ map has been

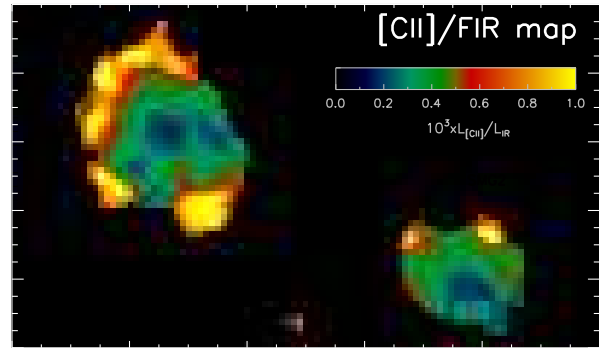


FIG. 6.— Resolved $L_{\text{[CII]}}/L_{\text{IR}}$ ratio map for our pair of SMGs. The L_{IR} for each pixel has been calculated from the observed flux density and using an extrapolation based on the median SED of SMGs in the ALESS survey (Swinbank et al. 2014), which produces a good fit to our photometric data points. The different morphology of dust and [CII] means that the [CII]/FIR ratio is higher in the outer parts of the galaxies and lower in the centre (where the peak of dust continuum emission is located). It should be noted that the yellow regions actually represent a lower limit of the $L_{\text{[CII]}}/L_{\text{IR}}$ ratio, since they correspond to regions where dust emission is not detected at $> 3\sigma$.

obtained from the [CII] moment-0 map by converting the line intensities in each pixel into line luminosities. The L_{IR} map has been derived from the observed $870\mu\text{m}$ dust continuum map by assuming the conversion from flux density to total IR luminosity at $z = 4.425$ derived from the average FIR SED of SMGs in ALESS (Swinbank et al. 2014), which is a good representation of the FIR SED of SGP38326.

The distinct dust and [CII] morphology leads to a complex spatial distribution for the [CII] to L_{IR} ratio (Fig. 6), which is higher in the outer parts of the two starbursts and lower in their centres, in agreement with what is observed for local LIRGs (Díaz-Santos et al. 2014). It should be noted that the yellow regions in Figure 6 indicate a lower limit for the $L_{\text{[CII]}}/L_{\text{IR}}$ ratio since they correspond to regions where dust continuum has not been detected, but where there is detectable [CII] emission (recall that [CII] is extended over a larger area than the dust, §3.4). Explaining the irregular morphology of the $L_{\text{[CII]}}/L_{\text{IR}}$ ratio is challenging due to the many phases of the ISM giving rise to [CII] emission (see §3.4). The most likely explanations are different excitation conditions for [CII] and variable dust optical depth across the disks. The presence of an AGN can also lower the $L_{\text{[CII]}}/L_{\text{IR}}$ ratio (Díaz-Santos et al. 2013), and so an AGN could therefore be responsible for the low values of the $L_{\text{[CII]}}/L_{\text{IR}}$ ratio in the center of the galaxies and in their integrated values (see below). While we have no direct evidence for an AGN with the present data, the existence of one would not be surprising since AGN seem to be ubiquitous in the strongest starbursts at lower redshifts (Ivison et al. 2013).

Larger samples of galaxies would be needed to explore at high resolution whether these gradients are present in most of the population of dusty starbursts at $z > 4$ and also in less extreme star forming systems.

Figure 7 compares the integrated values of the $L_{\text{[CII]}}/L_{\text{IR}}$ ratio with sources at similar redshifts and

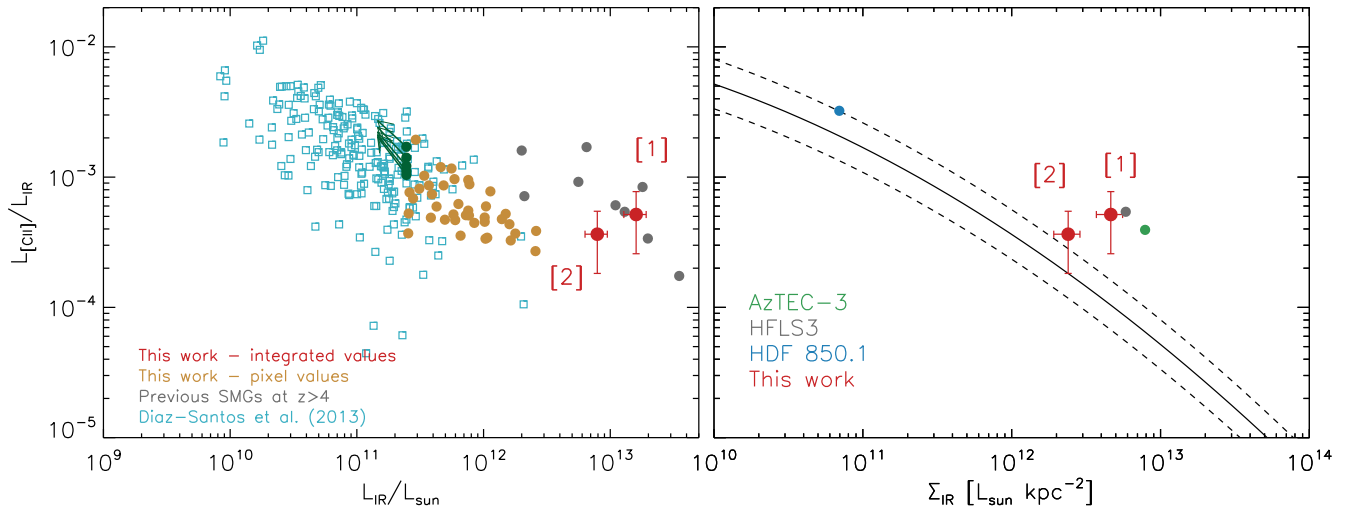


FIG. 7.— [CII] to L_{IR} ratio for our pair of interacting starbursts as a function of their total IR luminosity (*left*) and their IR surface density (*right*). On the left panel, the values for the two SMGs (SMG1 being [1] and SMG2 being [2]) in SGP38326 are shown with red filled dots and compared with previous results (grey dots) for submm galaxies at similar or higher redshifts (Swinbank et al. 2012; Walter et al. 2012; Riechers et al. 2013; Rawle et al. 2014; De Breuck et al. 2014; Riechers et al. 2014; Diaz-Santos et al. 2015) and with local IR-bright galaxies (Díaz-Santos et al. 2013). For lensed sources, the values included in the Figure has been corrected for amplification. We also represent the individual pixel values on the $L_{\text{[CII]}}/L_{\text{IR}}$ map (brown dots) after resampling the pixels to make them match with the size of the synthesized beam (see text for details). Green dots with arrows indicate upper limits of the $L_{\text{[CII]}}/L_{\text{IR}}$ and correspond to regions where there is [CII] emission but no dust continuum detection at 3σ . The IR luminosities in Díaz-Santos et al. (2013) have been converted to $L_{8-1000\mu\text{m}}$ by multiplying by a 1.8 factor. Our SMGs are on the bright side of the brightness distribution of previous SMGs with [CII] detections, and they also have amongst the lowest $L_{\text{[CII]}}/L_{\text{IR}}$ ratios. In the right panel, the black curve represents the best-fit for local galaxies in Lutz et al. (2015), with the dashed curves representing the scatter of the local relation. We compare the location of our two SMGs with dusty starbursts at similar or higher redshifts. Despite the small number of galaxies, there is an indication that galaxies with the highest SFR and star formation surface density (SMG1, AzTEC-3 and HFLS3) tend to depart from the local relation towards higher values of the $L_{\text{[CII]}}/L_{\text{IR}}$ ratio.

in the local Universe. The left panel of Figure 7 shows that the values found for the $L_{\text{[CII]}}/L_{\text{IR}}$ ratio in SMG1 and SMG2 are similar to those found in other comparably luminous IR galaxies at similar and higher redshifts (Swinbank et al. 2012; Walter et al. 2012; De Breuck et al. 2014; Riechers et al. 2014; Diaz-Santos et al. 2015) and in the local Universe (Díaz-Santos et al. 2013). Our two interacting starbursts are at the upper end of the L_{IR} distribution of $z > 4$ galaxies, suggesting that the anti-correlation between $L_{\text{[CII]}}/L_{\text{IR}}$ ratio and L_{IR} seen in the local Universe holds up to $z \sim 4$, but with an offset in L_{IR} .

We also present in Figure 7 the individual pixel values of the $L_{\text{[CII]}}/L_{\text{IR}}$ ratio for SMG1 and SMG2. Since the synthesized beam is sampled by approximately 5 pixels on each size, we have re-binned the $L_{\text{[CII]}}/L_{\text{IR}}$ ratio map every 5 pixels, so each new pixel approximately samples the area of one synthesized beam. Average values across contiguous pixels are taken during map re-sizing. For those regions with [CII] but no dust continuum detection we have given lower limits instead. The individual pixel values suggest that galaxy regions associated with higher star formation (or higher dust surface density) have lower $L_{\text{[CII]}}/L_{\text{IR}}$ ratios.

A tight correlation between the $L_{\text{[CII]}}/L_{\text{IR}}$ ratio and the IR surface density has been reported in local galaxies (Lutz et al. 2015). This relation and its typical scatter is represented in the right panel of Figure 7 along with the derived values for SMG1 and SMG2 and other $z > 4$ starbursts with measured sizes. We have defined the IR surface density as $\Sigma_{\text{IR}} = L_{\text{IR}}/(\pi R_a R_b)$, where R_a and R_b are the major and minor axis radii (derived by FWHM/2

from a elliptical gaussian profile) of the continuum dust emission of each galaxy.

Interestingly, the local relation holds, within the uncertainties, for SMG2 and also for other sources at $z > 4$. However, SMG1 and the most extreme sources at high redshift such as AzTEC-3 or HFLS3 depart from that relation, having $L_{\text{[CII]}}/L_{\text{IR}}$ ratios higher than the local relation for a given IR surface density. SMG1, AzTEC-3 and HFLS3 are close to the Eddington limit. This might indicate that the [CII] emission in those galaxies might be excited by an outflow. In fact, strong OH $163\mu\text{m}$ emission has been detected in AzTEC-3 and HFLS3 (Riechers et al. 2013, 2014), supporting the presence of outflowing material. However, no clear signature of OH $163\mu\text{m}$ emission or outflowing material (apart from the extended $^{12}\text{CO}(5-4)$ emission shown in Figure 2) has been detected in SMG1 (see §3.5), leaving unknown the reason of its enhanced $L_{\text{[CII]}}/L_{\text{IR}}$ ratio with respect to its IR surface density.

4. CONCLUSIONS

In this work we have presented ALMA high-spatial resolution ($\sim 0.1''$ or ~ 800 pc) imaging of the gas and dust in SGP38326, an interacting pair of IR-bright starburst at $z = 4.425$. Despite the redshift of the two galaxies being unknown when the ALMA $870\mu\text{m}$ continuum observations were defined, the [CII] and OH emission lines were luckily covered by the continuum spectral setup. This offered the opportunity of studying at high resolution the properties of the ISM in the likely progenitor of a massive, elliptical galaxy at $z \sim 3$. The main conclusions of our work are:

- The dust continuum emission (rest-frame $160\mu\text{m}$) in our pair of interacting starbursts at $z = 4.425$ presents a relatively smooth distribution at the resolution of our data and is distributed over an area of $2.2 \pm 0.2\text{kpc} \times 2.0 \pm 0.2\text{kpc}$ in SMG1 and $2.1 \pm 0.2\text{kpc} \times 1.5 \pm 0.1\text{kpc}$ in SMG2 (values quote FWHM of a 2D gaussian elliptical profile). However, the gas traced by [CII] emission has a more irregular morphology and is more extended than the gas, being extended over an area of $3.8 \pm 0.1\text{kpc} \times 2.9 \pm 0.1\text{kpc}$ in SMG1 and $2.7 \pm 0.1\text{kpc} \times 2.1 \pm 0.1\text{kpc}$ in SMG2.
- A dynamical analysis of the resolved [CII] emission revealed that the velocity fields of the two interacting components of SGP38326 are compatible with disk-like ordered rotation, in contrast with other extreme IR-bright starburst in the early Universe. The velocity field of the two interacting starbursts does not show any clear sign of outflowing material. In fact, the $163\mu\text{m}$ emission line (a tracer of molecular outflows), if present, is much fainter and narrower than in other extreme starbursts in the early Universe.
- Our high-resolution observations allowed us to build the first resolved $L_{[\text{CII}]} / L_{\text{IR}}$ map of a dusty starburst at $z > 4$. Due to the different morphologies of the dust and gas, the $L_{[\text{CII}]} / L_{\text{IR}}$ ratio is lower in the center of the galaxies and higher in the outer parts, where there is [CII] emission but no continuum is detected at $> 3\sigma$. This is consistent with what has been reported in the local Universe. The pixel values on the $L_{[\text{CII}]} / L_{\text{IR}}$ map suggest that regions with higher star formation have lower associated $L_{[\text{CII}]} / L_{\text{IR}}$ values.
- Our results support a scenario where the most distant starbursts were formed in the same highly dissipative mergers of gas-rich galaxies that seem ubiquitous amongst SMGs at $z < 3$, in agreement with recent simulation of IR-bright sources in the

early Universe.

Systems like SGP38326 are truly important to understand early massive galaxy formation. The SFR of SGP38326 will decline with an e -folding timescale of $\tau_{\text{gas}} \sim 100\text{Myr}$. This assumes a Salpeter IMF and $\tau_{\text{gas}} = 2 \times M(\text{H}_2) / \text{SFR}$, where the factor of two accounts for the 50% gas recycling in stellar evolution (Fu et al. 2013). This is a simplistic approach since it does not include the possible effect of gas outflow and inflow, but we can assume that they roughly compensate each other during galaxy growth (if there are strong outflows, τ_{gas} would be even lower). With that timescale, all the gas would have been consumed in $\sim 0.5\text{Gyr}$ (or $\sim 1\text{Gyr}$ if Chabrier IMF was assumed). Therefore, our extremely bright interacting starbursts are the likely progenitor of a massive elliptical at $z \sim 3$. We are, consequently, witnessing the formation of the red sequence of galaxies (Kriek et al. 2008).

IO, RJI, ZYZ, LD, AL and SM acknowledge support from the European Research Council in the form of the Advanced Investigator Programme, 321302, COSMICISM. IRS acknowledges support from STFC (ST/L00075X/1), the ERC Advanced Investigator programme DUSTYGAL 321334 and a Royal Society/Wolfson Merit Award. This paper makes use of the following ALMA data: ADS/JAO.ALMA#2013.1.00001.S and ADS/JAO.ALMA#2013.1.00449.S. ALMA is a partnership of ESO (representing its member states), NSF (USA) and NINS (Japan), together with NRC (Canada) and NSC and ASIAA (Taiwan) and KASI (Republic of Korea), in cooperation with the Republic of Chile. The Joint ALMA Observatory is operated by ESO, AUI/NRAO and NAOJ.” The *H-ATLAS* is a project with *Herschel*, which is an ESA space observatory with science instruments provided by European-led Principal Investigator consortia and with important participation from NASA. The *H-ATLAS* website is <http://www.h-atlas.org/>.

REFERENCES

- ALMA Partnership et al., 2015, ApJ, 808, L4
 Andrews B. H., Thompson T. A., 2011, ApJ, 727, 97
 Appleton P. N. et al., 2013, ApJ, 777, 66
 Appleton P. N. et al., 2015, ApJ, 812, 118
 Berta S., Lutz D., Genzel R., Foerster-Schreiber N. M., Tacconi L. J., 2015, ArXiv e-prints
 Blain A. W., Smail I., Ivison R. J., Kneib J.-P., Frayer D. T., 2002, Phys. Rep., 369, 111
 Bothwell M. S. et al., 2010, MNRAS, 405, 219
 Bussmann R. S. et al., 2013, ApJ, 779, 25
 Bussmann R. S. et al., 2015, ApJ, 812, 43
 Carilli C. L., Riechers D., Walter F., Maiolino R., Wagg J., Lentati L., McMahon R., Wolfe A., 2013, ApJ, 763, 120
 Carilli C. L., Walter F., 2013, ARA&A, 51, 105
 Casey C. M. et al., 2013, MNRAS, 436, 1919
 Chapman S. C., Blain A. W., Smail I., Ivison R. J., 2005, ApJ, 622, 772
 Ciccone C. et al., 2015, A&A, 574, A14
 Cooray A. et al., 2014, ApJ, 790, 40
 Dame T. M., 2011, ArXiv e-prints
 De Breuck C. et al., 2014, A&A, 565, A59
 Díaz-Santos T. et al., 2014, ApJ, 788, L17
 Díaz-Santos T. et al., 2013, ApJ, 774, 68
 Díaz-Santos T. et al., 2015, ArXiv e-prints
 Downes D., Solomon P. M., 1998, ApJ, 507, 615
 Dunne L., Eales S. A., 2001, MNRAS, 327, 697
 Dye S. et al., 2015, MNRAS, 452, 2258
 Eales S. et al., 2010, PASP, 122, 499
 Edge A., Sutherland W., Kuijken K., Driver S., McMahon R., Eales S., Emerson J. P., 2013, The Messenger, 154, 32
 Elbaz D. et al., 2011, A&A, 533, A119
 Engel H. et al., 2010, ApJ, 724, 233
 Farrah D. et al., 2013, ApJ, 776, 38
 Förster Schreiber N. M. et al., 2009, ApJ, 706, 1364
 Fu H. et al., 2013, Nature, 498, 338
 Gabor J. M., Davé R., 2012, MNRAS, 427, 1816
 Geach J. E. et al., 2013, MNRAS, 432, 53
 Genzel R. et al., 2014, ApJ, 785, 75
 Hartley W. G. et al., 2013, MNRAS, 431, 3045
 Hodge J. A., Carilli C. L., Walter F., de Blok W. J. G., Riechers D., Daddi E., Lentati L., 2012, ApJ, 760, 11
 Hodge J. A. et al., 2013, ApJ, 768, 91
 Hodge J. A., Riechers D., Decarli R., Walter F., Carilli C. L., Daddi E., Dannerbauer H., 2015, ApJ, 798, L18
 Holland W. S. et al., 2013, MNRAS, 430, 2513
 Hwang H. S. et al., 2010, MNRAS, 409, 75
 Ikarashi S. et al., 2015, ApJ, 810, 133

- Iverson R. J., Papadopoulos P. P., Smail I., Greve T. R., Thomson A. P., Xilouris E. M., Chapman S. C., 2011, *MNRAS*, 412, 1913
- Iverson R. J. et al., 2013, *ApJ*, 772, 137
- Karim A. et al., 2013, *MNRAS*, 432, 2
- Kennicutt, Jr. R. C., 1998, *ARA&A*, 36, 189
- Kodama T., Tanaka I., Kajisawa M., Kurk J., Venemans B., De Breuck C., Vernet J., Lidman C., 2007, *MNRAS*, 377, 1717
- Kriek M., van der Wel A., van Dokkum P. G., Franx M., Illingworth G. D., 2008, *ApJ*, 682, 896
- Leroy A. K. et al., 2011, *ApJ*, 737, 12
- Lutz D. et al., 2015, *ArXiv e-prints*
- Madden S. C., Poglitsch A., Geis N., Stacey G. J., Townes C. H., 1997, *ApJ*, 483, 200
- Magdis G. E. et al., 2012, *ApJ*, 760, 6
- Magdis G. E. et al., 2011, *ApJ*, 740, L15
- Mei S. et al., 2009, *ApJ*, 690, 42
- Narayanan D. et al., 2015, *Nature*, 525, 496
- Oke J. B., Gunn J. E., 1983, *ApJ*, 266, 713
- Oliver S. J. et al., 2010, *A&A*, 518, L21
- Oteo I., Zwaan M. A., Iverson R. J., Smail I., Biggs A. D., 2015, *ArXiv e-prints*
- Rawle T. D. et al., 2014, *ApJ*, 783, 59
- Riechers D. A. et al., 2013, *Nature*, 496, 329
- Riechers D. A. et al., 2014, *ApJ*, 796, 84
- Rosati P. et al., 2009, *A&A*, 508, 583
- Rowlands K. et al., 2014, *MNRAS*, 441, 1017
- Sandstrom K. M. et al., 2013, *ApJ*, 777, 5
- Scoville N. et al., 2015, *ArXiv e-prints*
- Simpson J. M. et al., 2015a, *ApJ*, 799, 81
- Simpson J. M. et al., 2015b, *ApJ*, 807, 128
- Siringo G. et al., 2009, *A&A*, 497, 945
- Sobral D., Smail I., Best P. N., Geach J. E., Matsuda Y., Stott J. P., Cirasuolo M., Kurk J., 2013, *MNRAS*, 428, 1128
- Solomon P. M., Downes D., Radford S. J. E., Barrett J. W., 1997, *ApJ*, 478, 144
- Stacey G. J. et al., 1999, in *ESA Special Publication*, Vol. 427, *The Universe as Seen by ISO*, Cox P., Kessler M., eds., p. 973
- Stanford S. A. et al., 2006, *ApJ*, 646, L13
- Strazzullo V. et al., 2010, *A&A*, 524, A17
- Swinbank A. M. et al., 2015, *ApJ*, 806, L17
- Swinbank A. M. et al., 2012, *MNRAS*, 427, 1066
- Swinbank A. M. et al., 2014, *MNRAS*, 438, 1267
- Symeonidis M. et al., 2013, *MNRAS*, 431, 2317
- Tacconi L. J. et al., 2008, *ApJ*, 680, 246
- Tacconi L. J. et al., 2006, *ApJ*, 640, 228
- Thomas D., Maraston C., Bender R., Mendes de Oliveira C., 2005, *ApJ*, 621, 673
- Thomas D., Maraston C., Schawinski K., Sarzi M., Silk J., 2010, *MNRAS*, 404, 1775
- Toomre A., 1964, *ApJ*, 139, 1217
- Tozzi P. et al., 2015, *ApJ*, 799, 93
- Walter F. et al., 2012, *Nature*, 486, 233
- Walter F., Riechers D., Cox P., Neri R., Carilli C., Bertoldi F., Weiss A., Maiolino R., 2009, *Nature*, 457, 699
- Weiß A. et al., 2009, *ApJ*, 707, 1201
- Wolfire M. G., Hollenbach D., McKee C. F., 2010, *ApJ*, 716, 1191
- Zhu M., Gao Y., Seaquist E. R., Dunne L., 2007, *AJ*, 134, 118
- Zirm A. W. et al., 2008, *ApJ*, 680, 224